Hindawi
International Journal of Aerospace Engineering
Volume 2023, Article ID 5541338, 9 pages
https://doi.org/10.1155/2023/5541338

Research Article

A Pulsar Vector Observation-Based Link Acquisition Method for X-Ray Communications

Shibin Song, Xiao Lu, and Haixia Wang

Key Laboratory for Robot & Intelligent Technology of Shandong Province, Shandong University of Science and Technology, Qingdao 266590, China

Correspondence should be addressed to Shibin Song; shbsong_skd@sdust.edu.cn

Received 24 March 2023; Revised 15 August 2023; Accepted 25 November 2023; Published 14 December 2023

Academic Editor: Chuang Liu

X-ray communication (XCOM) is an emerging laser communication technique for deep space applications. Traditional link acquisition of laser communications depends significantly on Earth support and shows little autonomy. For XCOM, a pulsar vector observation-based link acquisition method is proposed, which utilizes noncooperative pulsars in deep space as beacons to acquire absolute attitude information and accomplish link acquisition. Firstly, a pulsar vector observation model was established based on the coordinate definition of the X-ray detector and X-ray collimator model. Secondly, a modified "success-failure" pulsar vector search algorithm with two degrees of freedom was proposed to acquire the pulsar vector. With the pulsar vector and the relative attitude obtained from inertial sensors, the link acquisition pointing vector could be determined. Finally, the performance of the proposed method was evaluated using numerical experiments, and factors that influence the performance are discussed and analyzed.

1. Introduction

X-ray communication (XCOM) is a revolutionary technique in space communication [1, 2], which takes advantage of the high energy and excellent penetrative properties of X-rays in deep space [3, 4] and is widely studied. In China, Zhao et al. first discussed the application of X-rays in space communication [5]. Zhao et al. extensively studied various aspects of XCOM, including transmission properties [6], frequency modulation [7], source design and testing [8–10], and XCOM applications [11–13]. These studies built a solid foundation for XCOM development. In addition, Tang et al. conducted a series of studies regarding XCOM, including the penetrative properties of X-rays [14], X-ray high frequency pulse emission characteristics [15], and collimating/focusing optical systems [16]. The potential applications of XCOM in the Mars scenario [3, 17] and during Earth reentry [18–20] were also studied. These studies remarkably promoted the development of XCOM.

Though extensive research has been performed, the study of XCOM is ongoing and many problems remain unsolved. X-ray signal modulation, communication signal denoising, X-ray detector design and optimization, communication link acquisition, and establishment are main technical challenges for XCOM. X-ray transmission properties, X-ray source and detector design, and X-ray signal modulation are studied by researchers. Of current challenges, there is no literature concerning link acquisition of XCOM for deep space applications. In traditional laser communication, a master/slave pattern [21] is commonly used for link acquisition, which establishes an extra optical link between a transmitter (master) and a receiver (slave) [22], and the communication link acquisition is established by acquiring the beacon link between the master and slave station. The traditional acquisition system depends greatly on the beacon link and is time-consuming and complicated, and extra equipment is required for the beacon link. In addition, the beacon link is easily affected by other optical sources in deep space.

To eliminate the dependence on the beacon link and improve autonomy, a pulsar vector observation-based acquisition method is proposed. Pulsars are neutron stars in space

and emit signals over a wide spectrum, which include radio waves, visible light, X-rays, and gamma rays [23, 24]. Of the emitted signals, X-ray pulsar signals show low attenuation and good radiation directivity [25, 26], making them suitable for attitude determination [27]. As regards the proposed acquisition method, pulsars serve as noncooperative beacons, and a pulsar vector observation method is proposed to acquire an accurate absolute attitude. With other supplementary information, such as the pulsar ephemeris, positions obtained from the navigation system, and other data, the link acquisition can be established. Compared with the master/slave pattern, the link acquisition reflected in this paper uses noncooperative pulsars as beacons and eliminates the dependence on the beacon link, providing a simple and autonomous method of link acquisition for XCOM. The main contribution of this research is that a pulsar vector observation-based XCOM link acquisition method is proposed, which utilizes X-ray pulsars in deep space as beacons and can establish X-ray communication link without extra optical link. This research paves a new way for XCOM link acquisition and contributes to the development of XCOM. Besides, the proposed approach can be potentially used in attitude system control. In the threatening space environment, attitude determination is vital for spacecraft navigation and communication, and accurate control of spacecraft attitude system is quite important [28]. The proposed approach could obtain attitude information based on pulsar signals. This attitude information depends on pulsar signals and is barely influenced by equipment drift, equipment noise, etc., which contributes to the better control of spacecraft attitude system.

2. Basic Concepts

Figure 1 presents the relation between the pulsar vector and the line of sight (LOS) of the XCOM link. In the figure, A and B are the communication terminals on different spacecraft, $\mathbf{n}$ denotes the unit vector of the pulsar signal radiation direction, and $\mathbf{p}$ is the desired pointing vector for XCOM link alignment. Let $\tilde{\mathbf{n}}$ be the observation of $\mathbf{n}$ and θ be the pulsar observation error. If γ denotes the error between $\mathbf{p}$ and its observation $\tilde{\mathbf{p}}$, γ can be used to evaluate the acquisition error.

Assuming the remote end (terminal B) is a spacecraft, the pulsar vector $\mathbf{n}$ can be observed through a pulsar vector observation system. The relation between the pulsar vector observation system and the spacecraft can be measured by the spacecraft's onboard inertial sensors. The position of terminal B can be estimated by an X-ray pulsar-based navigation (XPNAV) system [29, 30]. Assuming the proximal end (terminal A) is a satellite and the position of terminal A is known, then, the pointing vector of the XCOM link can be estimated with the obtained information.

3. Pulsar Vector Observation Model

3.1. Coordinate Definition. The pulsar vector represents the direction of radiation of pulsar signals. A pulsar vector can be observed by acquiring X-ray photons with an X-ray detector. Collimators are well-type pipes, which are placed in front of an X-ray detector to mitigate background noises [31]. The X-ray detector is placed on a two-degree of freedom pan-tilt mechanism, and by controlling the rotation of the mechanism, the pointing direction of the detector and collimator is adjusted.

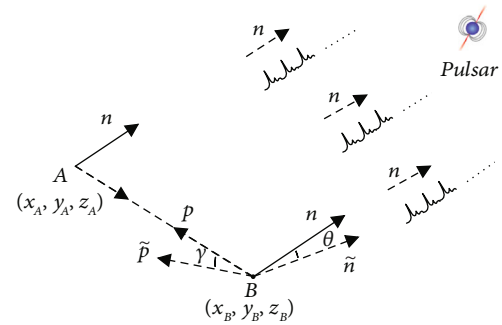

Figure 1: Relation between the pulsar vector and the LOS of the XCOM link.

To describe the pulsar vector observation process, a detector/collimator coordinate system should be defined. In addition, the body-fixed coordinate system of the spacecraft where the X-ray detector is placed should also be considered. Figure 2 presents the collimator coordinate system (C-coordinate) and the body-fixed coordinate system (B-coordinate). The C-coordinate is denoted by $O - x_c y_c z_c$. x_c is the central axis of the collimator. $x_c O y_c$ forms the bottom plane of the collimator, and x_c, y_c, and z_c form a right-handed coordinate system. Let $\mathbf{n}$ be the radiation direction of X-ray pulsar signals and the angle error between $\mathbf{n}$ and z_c be denoted by δ.

The B-coordinate is a fundamental coordinate for a spaceborne system. In Figure 2, the B-coordinate is denoted by $O - x_b y_b z_b$. The origin of the B-coordinate is generally at the barycenter of the spacecraft. As indicated in Figure 2, x_b is along the longitudinal axis of the spacecraft and z_b is vertical to the longitudinal plane of the spacecraft. x_b, y_b, and z_b form a right-handed coordinate system.

Assuming that the B-coordinate and C-coordinate share the same origin, the relation between the two coordinate systems can be expressed by the angles α and β. α is the horizontal rotation angle of the C-coordinate relative to the B-coordinate. β denotes the rotation angle of the $x_c o y_c$ plane relative to the $x_b o y_b$ plane. α can be calculated from the angle between x_b and the projection of x_c on plane $x_b o y_b$. β can be obtained from the angle between z_c and the projection of z_c on plane $x_b o y_b$.

3.2. Pulsar Observation Model. Collimators are elongated wells placed in front of an X-ray detector. When observing X-ray pulsar signals, the incident X-ray photons that deviate from the collimator direction will hit the collimators' sidewalls and not reach the detector. Thus, the pulsar vector observation result is closely related to the collimator model and direction.

Given its geometrical shape, a collimator can be regarded as a cylinder [32]. A model of a collimator is presented in

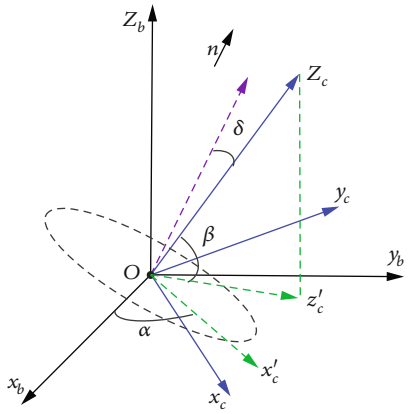

Figure 2: Definition of coordinate systems.

Figure 3. In Figure 3, r represents the radius of the collimator, h is the length of the collimator, and **n** is the pulsar vector. The effective area of the X-ray detector is defined as the area where X-ray pulsar signals can be detected by the detector after traveling through the collimators. When there is an error angle δ between z_c and **n**, the effective area is smaller than the collimators' bottom area. According to the geometrical relation shown in Figure 3, δ satisfies

$$\delta = \arctan\left(\frac{l_1}{h}\right). \tag{1}$$

Notably, when $\delta > \arctan(2r/h)$, the effective area becomes 0. Thus, the range of δ is limited to $[0, \arctan(2r/h))$.

As indicated in Figure 3, the solid line circle is the bottom of a collimator and the dotted line circle is the ideal photo arrival area. When $\delta = 0$, the solid line circle and the dotted line circle are totally overlapped.

As δ increases, parts of photons hit the side wall of the collimator and cannot reach the collimator bottom. The effective photon arrival area is the overlap area of the solid line circle and the dotted line circle. When δ is small $(0 < \delta < \arctan(r/h))$, the center of the solid line circle is covered by the effective area, which is case (b) in Figure 4. When δ increases $(\arctan(r/h) < \delta < \arctan(2r/h))$, the effective area is case (a) in Figure 4. The diamond drawn in Figure 4 case (b) is used to calculate the area of the shadow part.

Thus, the calculation of X-ray detector effective area can be divided into two cases: case (a) of $\arctan(r/h) < \delta < \arctan(2r/h)$ shown in Figure 4(a) and case (b) of $0 < \delta < \arctan(r/h)$ shown in Figure 4(b).

For case (a), as l_1 can be expressed by $l_1 = h \tan\delta$, l can be calculated by

$$l = 2r - l_1 = 2r - h\tan\delta. \tag{2}$$

For case (b), there is

$$l = 2r - l_1 - 2(r - l_1) = l_1. \tag{3}$$

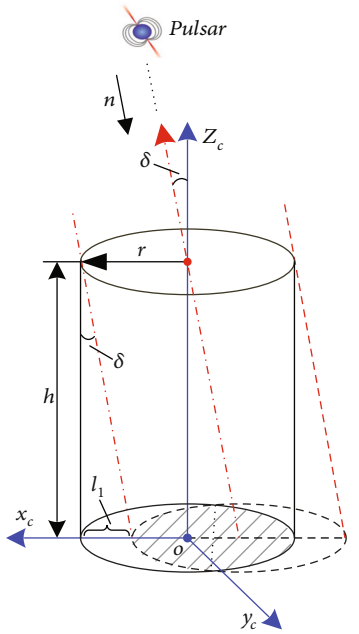

Figure 3: Collimator model.

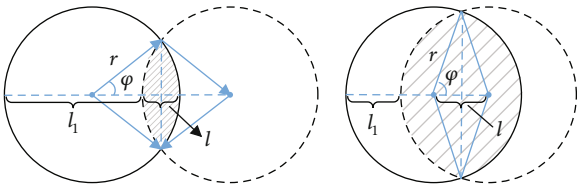

(a) $\arctan(r/h) < \delta < \arctan(2r/h)$ (b) $0 < \delta < \arctan(r/h)$

Figure 4: The effective area definition.

Therefore, for case (a), the effective area is expressed by

$$S_e(\delta) = 2\left[\frac{1}{2}r^2(2\varphi) - \frac{1}{2}(2r\sin\varphi)\left(r - \frac{l}{2}\right)\right], \tag{4}$$

where δ satisfies

$$\cos\varphi = \frac{r - l/2}{r} = \frac{h\tan\delta}{2r},$$
$$\sin\varphi = \frac{\sqrt{4r^2 - h^2\tan^2\delta}}{2r}. \tag{5}$$

With Eq. (5), Eq. (4) can be rewritten as

$$\begin{aligned} S_e(\delta) &= 2r^2\varphi - 2\left(r - \frac{l}{2}\right)r\sin\varphi \\ &= 2r^2\varphi - \frac{h\tan\delta\sqrt{4r^2 - h^2\tan^2\delta}}{2} \\ &= 2r^2\ \arcsin\left(\frac{\sqrt{4r^2 - h^2\tan^2\delta}}{2r}\right) \\ &\quad - \frac{h\tan\delta\sqrt{4r^2 - h^2\tan^2\delta}}{2}. \end{aligned} \tag{6}$$

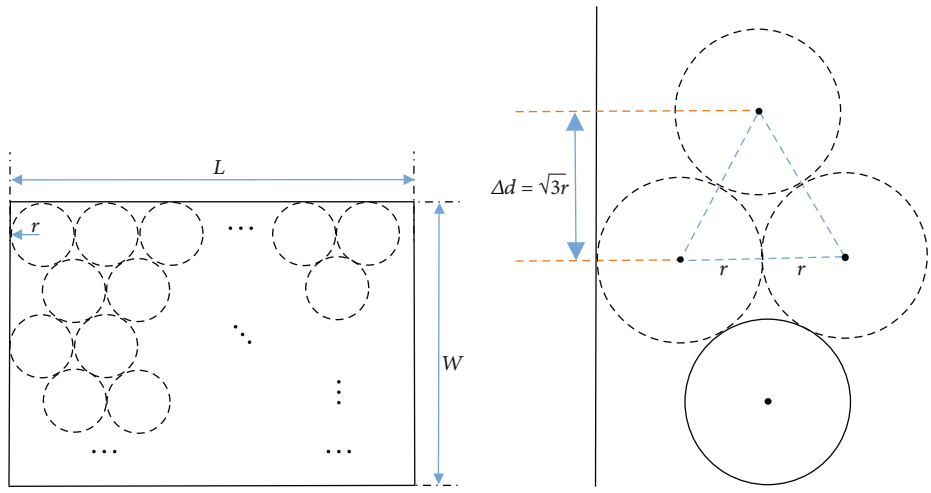

(a) Collimator layout (b) Geometric dimensioning of collimator layout

Figure 5: Layout of collimators on a detector.

Rotate $\mathbf{n}_{zc0}$ *around* z_b *by* s_1, *and obtain a new pointing vector* $\mathbf{n}_{zc1}$.
Calculate the cross product of $\mathbf{n}_{zc1}$ *and* z_b, *which is denoted by* $\mathbf{n}_{tmp}$.
Rotate $\mathbf{n}_{zc1}$ *by* s_2 *around* $\mathbf{n}_{tmp}$, *and obtain a new pointing vector,* $\mathbf{n}_{zc2}$.
At $\mathbf{n}_{zc2}$, *obtain* Ph_2 *based on Eq.*(13).
If $Ph_2 > Ph_0$
  Then, let $s_1 = 2s_1$ *and* $s_2 = 2s_2$
  Turn to step 10
Else
  Rotate $\mathbf{n}_{zc0}$ *around* z_b *by* s_1, *and obtain a pointing vector* $\mathbf{n}_{zc1}$.
  Calculate the cross product of $\mathbf{n}_{zc1}$ *and* z_b, *denoted by* $\mathbf{n}_{tmp}$.
  Rotate $\mathbf{n}_{zc1}$ *by* $-s_2/4$ *around* $\mathbf{n}_{tmp}$ *and obtain a new pointing vector,* $\mathbf{n}_{zc2}$.
  At $\mathbf{n}_{zc2}$, *obtain* Ph_2 *based on Eq.*(13).
    If $Ph_2 > Ph_0$
      Then, let $s_1 = s_1$ *and* $s_2 = -s_2/2$.
      Turn to step 10.
    Else
      Rotate $\mathbf{n}_{zc0}$ *around* z_b *by* $-s_1/4$, *and obtain a pointing vector* $\mathbf{n}_{zc1}$.
      Calculate the cross product of $\mathbf{n}_{zc1}$ *and* z_b, *denoted by* $\mathbf{n}_{tmp}$.
      Rotate $\mathbf{n}_{zc1}$ *by* s_2, *and obtain a new pointing vector,* $\mathbf{n}_{zc2}$.
      At $\mathbf{n}_{zc2}$, *obtain* Ph_2 *based on Eq.*(13).
        If $Ph_2 > Ph_0$
          Then, let $s_1 = -s_1/2$ *and* $s_2 = s_2$.
          Turn to step 10
        Else
          Rotate $\mathbf{n}_{zc0}$ *around* z_b *by* $-s_1/4$, *and obtain a pointing vector* $\mathbf{n}_{zc1}$.
          Calculate the cross product of $\mathbf{n}_{zc1}$ *and* z_b, *denoted by* $\mathbf{n}_{tmp}$.
          Rotate $\mathbf{n}_{zc1}$ *by* $-s_2/4$, *and obtain a new pointing vector,* $\mathbf{n}_{zc2}$.
          At $\mathbf{n}_{zc2}$, *obtain* Ph_2 *based on Eq.*(13).
          Let $s_1 = -s_1/2$ *and* $s_2 = -s_2/2$.
          Turn to step 10
If $|s_1| < \varepsilon$ *and* $|s_2| < \varepsilon$
  Then, end the search.
Else
  $Ph_0 = Ph_2$, *and* $\mathbf{n}_{zc0} = \mathbf{n}_{zc2}$.
  Turn to step 1.

Algorithm 1: Pulsar vector search algorithm.

Similarly, for case (b), we get

$$\begin{aligned} S_e(\delta) &= 2\left[\frac{1}{2}r^2(2\varphi) - 2\left(\frac{1}{2}\frac{l}{2}r\sin\varphi\right)\right] \\ &= 2r^2\varphi - lr\sin\varphi \\ &= 2r^2\arcsin\left(\frac{\sqrt{4r^2 - h^2\tan^2\delta}}{2r}\right) \\ &\quad - \frac{h\tan\delta\sqrt{4r^2 - h^2\tan^2\delta}}{2}. \end{aligned} \tag{7}$$

Based on the above analysis, the effective area of a collimator can be described by

$$S_e(\delta) = \begin{cases} 2r^2\arcsin(\Lambda) - \Omega, & 0 < \delta < \arctan\left(\frac{2r}{h}\right), \\ 0, & \text{others}, \end{cases} \tag{8}$$

where

$$\begin{aligned} \Lambda &= \frac{\sqrt{4r^2 - h^2\tan^2\delta}}{2r}, \\ \Omega &= \frac{h\tan\delta\sqrt{4r^2 - h^2\tan^2\delta}}{2}. \end{aligned} \tag{9}$$

Then, for a single collimator, the photo intensity received by the detector can be expressed by

$$\mathrm{ph}_f = \eta S_e(\delta)\Lambda, \tag{10}$$

where η is the detection efficiency and Λ is the average flux intensity of the incident X-ray signals.

As the collimators are cylinders with a round bottom, the full area of the detector cannot be used. Figure 5(a) shows the layout of the collimators, and Figure 5(b) indicates the geometric dimensioning of collimator layout. Assume that the width of the detector is W and the length L. Along the widthwise direction, the number of collimators allowed is $k = \lfloor (W - 2r)/\sqrt{3r} \rfloor + 1$, where the symbol $\lfloor \quad \rfloor$ depicts rounding half down. If k is an even number, the number of collimators for a detector of $L * W$ is

$$N_p = \left\lfloor \frac{L}{2r} \right\rfloor * k - \frac{k}{2}. \tag{11}$$

If k is an odd number, the number of collimators is

$$N_p = \left\lfloor \frac{L}{2r} \right\rfloor * k - \frac{k-1}{2}. \tag{12}$$

Using Eq. (9), the photo intensity received by the entire detector can be presented as

$$\mathrm{PH}_f = \eta S_e \Lambda N_p. \tag{13}$$

Table 1: Pulsar parameters.

Parameters	Values
Pulsars	B0531+21
Period (s)	3.34*e*-2
Right ascension (rad)	1.45967
Declination (rad)	0.3847
Flux intensity (ph/cm^2/s)	1.54
Pulse width (s)	3.0*e*-3
Pulsed fraction (%)	70

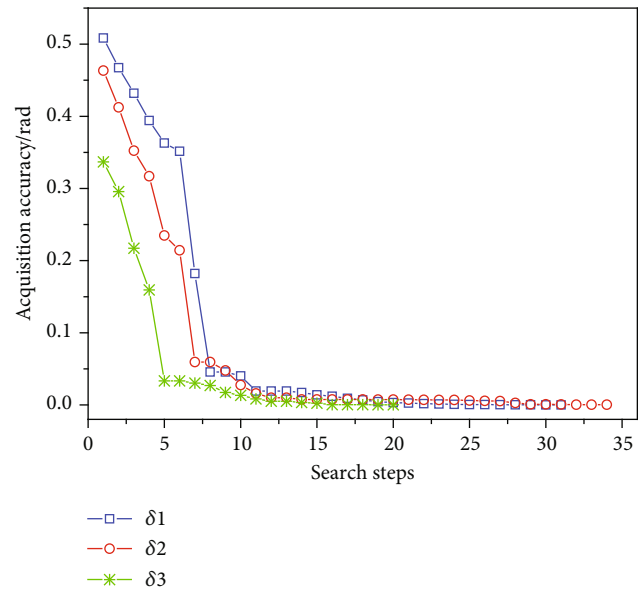

Figure 6: Link acquisition simulation.

Besides, to guarantee the precision of the measurement, X-ray detector calibration and noise filtering should be considered. An X-ray detector calibration can be realized using "two-point calibration" [33]. For the calibration method, two scaling points, φ_1 and φ_2, are set. φ_1 represents the received energy when X-ray emitting source is turned off, and φ_2 represents the received energy when X-ray emitting source is turned on. Under the two scaling points, the output signals of X-ray sense components are obtained. The output signals are used to calculate the offset parameter and gain parameter of X-ray sense components.

Though collimators can mitigate some background noises, there are still noise signals arriving at the detector. Through numerical experiments using date from on-orbit X-ray detector, the Wiener filter shows good filtering performance for the proposed method.

4. Pulsar Vector Observation

Pulsar vector observation is the determination of the radiation direction of X-ray pulsar signals, which is realized by adjusting the direction of the collimators. Based on the

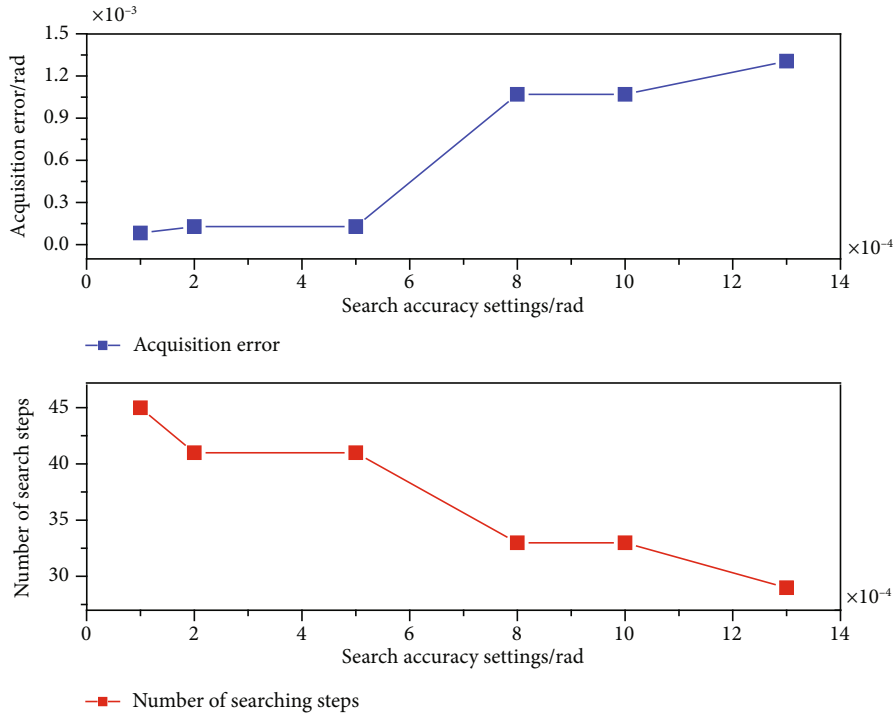

FIGURE 7: Search results under different search accuracy settings.

pulsar observation model, a pulsar vector search algorithm with two degrees of freedom is proposed.

The search algorithm is inspired by the "success-failure method" and is conducted using two degrees of freedom. For a complete search attempt, the α and β directions are found by rotating the collimator direction along the α and β directions, respectively. To describe the rotation of a vector, the quaternion is used. Assuming that $\mathbf{n}_0 = (n_{0x}, n_{0y}, n_{0z})$ rotates around the rotation axis $\mathbf{n}_r$ and that θ_r is the rotation angle, a quaternion can be expressed by

$$q = \cos\left(\frac{\theta_r}{2}\right) + \sin\left(\frac{\theta_r}{2}\right)\left(n_{0x}i + n_{0y}j + n_{0z}k\right), \tag{14}$$

where i, j, and k are imaginary units. Utilizing a quaternion to express $\mathbf{n}_0$ gives

$$v = 0 + \left(n_{0x}i + n_{0y}j + n_{0z}k\right). \tag{15}$$

Then, the rotation process can be expressed by

$$L = qvq^*, \tag{16}$$

where q^* is the conjugate of q. The rotation result is the conjugate transformation of L.

Let $\mathbf{n}_{zc}$ denote the direction of z_c. Set s_1 and s_2 to be the search step of the α and β directions, respectively. $\mathbf{n}_{zc0}$ denotes the initial direction of $\mathbf{n}_{zc}$, and the observed photon flux intensity at this attitude is Ph_0. Let the search accuracy to be set to ε, which is used to terminate the search algorithm. The detailed search algorithm can be described in pseudocode in Algorithm 1.

At the proximal end (terminal A), $\mathbf{n}_A$ is obtained by the proposed pulsar vector observation method, and the rotation relation between the pointing vector of its communication terminal and the pulsar vector $\mathbf{n}_A$ is known between the two terminals. At the remote end (terminal B), the pulsar vector $\mathbf{n}_B$ can also be obtained by the proposed pulsar vector observation method. Using this information, the pointing vector $\mathbf{n}_c$ of link acquisition at the remote end (terminal B) can be estimated.

As the acquisition error is related to the pulsar vector observation error, the acquisition error is expressed by

$$\cos\delta = \frac{\mathbf{n}_c \cdot \mathbf{n}_B}{|\mathbf{n}_c||\mathbf{n}_B|}, \tag{17}$$

where $\mathbf{n}_c$ is the pointing vector of the collimators and $\mathbf{n}_B$ is the pulsar vector observed at the remote end (terminal B).

5. Experiment Results

5.1. Simulation Conditions. To evaluate the performance of the proposed acquisition method, a series of numerical simulations was conducted. For the simulation, the size of the X-ray detector was set to $1\,\mathrm{m}^2$. The background flux intensity was set to be $5e\text{-}3\,\mathrm{ph/cm}^2/\mathrm{s}$. The parameters of the pulsar are listed in Table 1.

5.2. Link Acquisition Simulation. The link acquisition procedure was simulated in this section. For simulation conditions, the search accuracy was set to be $\varepsilon = 2e-4\,\mathrm{rad}$, and

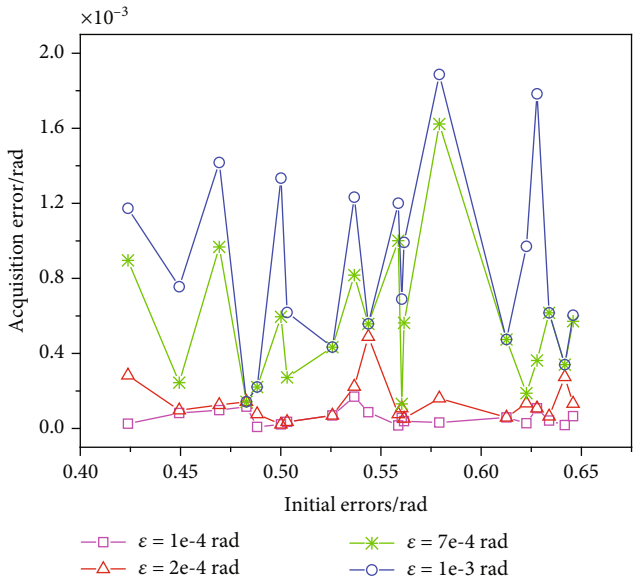

Figure 8: Acquisition error analysis.

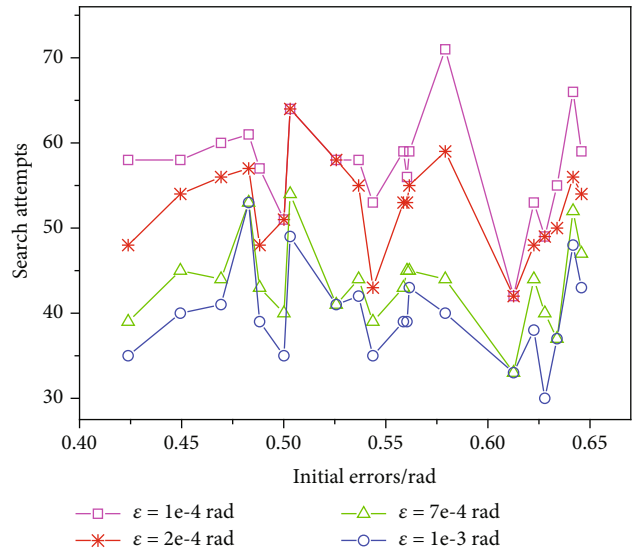

Figure 9: Search attempt analysis.

the initial searching step was set as $s_1 = s_2 = \text{pi}/2$. To simulate different initial pointing directions of the collimators, the initial error, δ, was set to different values.

In Figure 6, the horizontal axis denotes the search attempts required during the search procedure, and the vertical axis is the link acquisition error. As can be seen in Figure 6, the acquisition error decreases almost to zero, but not monotonously. The reason is that not all search attempts are successful during the search procedure. When searching in the wrong direction, the acquisition error will deviate from the decreasing trend.

5.3. Acquisition Error Analysis. In this section, the acquisition error is analyzed by numerical experiments. The search procedure was simulated under different search accuracy settings, $\varepsilon = [1e-4, 2e-4, 4e-4, 7e-4, 8e-4, 1e-3]$, and the same initial pointing error δ.

Figure 7 presents the acquisition error and the number of search steps required under the simulated conditions, and it can be seen that with a smaller search accuracy set, a better acquisition error is obtained. However, more search attempts are required during the search procedure. Thus, when choosing search accuracy settings, the balance between the acquisition error and the number of search attempts should be considered.

5.4. Influences of the Initial Errors and the Search Accuracy Settings. The influence of the initial pointing error δ and the search accuracy setting ε on the acquisition performance is analyzed in this section.

Figure 8 presents the acquisition errors using different search accuracy settings and initial pointing errors. In Figure 8, the horizontal axis represents different initial pointing errors, and the vertical axis represents the acquisition errors. It is shown from Figure 8 that for a given search accuracy, the initial error has little impact on the acquisition error results. Moreover, with smaller search accuracy settings, better acquisition errors are obtained.

Figure 9 shows the number of search attempts required under different search accuracy settings and initial pointing errors. The axis definitions are the same as that of Figure 8. As indicated in Figure 9, the number of search attempts required shows little connection with the initial errors. This is because during the search procedure, the search steps s_1 and s_2 are dynamically changing after each search attempt. It is shown in the figure that with a smaller search accuracy, more search attempts are required for the proposed acquisition system.

6. Conclusions

In this paper, a pulsar vector observation-based XCOM link acquisition method is presented. A pulsar vector observation model was established based on the collimator model and coordinate definition, and a pulsar vector search method is proposed. With pulsar vector observation and prior knowledge, the link acquisition vector could be obtained. Numerical experiments indicated that the proposed method could gradually obtain the acquisition pointing vector, and the search accuracy settings directly influence the acquisition accuracy and number of search attempts required. Using noncooperative pulsars as beacons, the proposed vector observation-based link acquisition method provides a more independent way of XCOM link acquisition, contributing to the further application of XCOM in deep space.

Data Availability

The simulation data used to support the findings of this study are available from the corresponding author upon request.

Conflicts of Interest

The authors declare that there is no conflict of interest regarding the publication of this paper.

Acknowledgments

The authors would like to thank Hua Zhang of Xidian University for helpful discussions on topics related to this work. This work was supported by the National Natural Science Foundation of China (62103245 and 62273213), the Natural Science Foundation of Shandong Province (ZR2020MF095), and Taishan Scholarship Construction Engineering.

References

[1] L. M. Jin, W. B. Jia, D. Q. Hei, L. Zhao, and C. Cheng, "Feasibility study of the high frequency X-ray communication using selective characteristic X-rays," *Optics Communications*, vol. 484, article 126697, 2021.

[2] National Research Council, *NASA Space Technology Roadmaps and Priorities: Restoring NASA's Technological Edge and Paving the Way for a New Era in Space*, The National Academies Press, Washington, DC, United States, 2012.

[3] S. Hang, X. B. Tang, H. Li et al., "Potential application of X-ray communication in Martian dust storm," *Acta Astronautica*, vol. 166, pp. 277–289, 2020.

[4] Y. Li, T. Su, L. Z. Sheng, P. F. Qiang, N. Xu, and B. S. Zhao, "X-ray transmission characteristics and potential communication in re-enter plasma sheath," *Optik*, vol. 197, article 162917, 2019.

[5] B. S. Zhao, C. X. Wu, L. Z. Sheng, and Y. A. Liu, "Next generation of space wireless communication technology based on X-ray," *Acta Photonica Sinica*, vol. 42, no. 7, pp. 801–804, 2013.

[6] L. Q. Wang, T. Su, B. S. Zhao, L. Z. Sheng, Y. A. Liu, and D. Liu, "Bit error rate analysis of X-ray communication system," *Acta Physica Sinica*, vol. 64, no. 12, pp. 119–123, 2015.

[7] T. Su, L. Y. Tang, Y. Li, L. Z. Sheng, and B. S. Zhao, "An X-ray frequency modulation method and its application in X-ray communication," *Optik*, vol. 199, article 163263, 2019.

[8] Y. A. Liu, H. Xuan, L. Z. Sheng et al., "X-ray communication experiment using photocathode X-ray tube," in *7th Symposium on Novel Photoelectronic Detection Technology and Applications*, Kunming, China, 2021.

[9] D. Liu, P. F. Qiang, L. S. Li et al., "X-ray focusing optics and its application in X-ray communication system," *Acta Physica Sinica*, vol. 65, no. 1, pp. 71–76, 2016.

[10] X. F. Ma, B. S. Zhao, L. Z. Sheng, Y. A. Liu, D. Liu, and N. Q. Deng, "Grid-controlled emission source for space X-ray communication," *Acta Physica Sinica*, vol. 63, no. 16, pp. 81–87, 2014.

[11] N. Q. Deng, B. S. Zhao, L. Z. Sheng, Q. R. Yan, H. Yang, and D. Liu, "A space audio cummunication system based on X-ray," *Acta Physica Sinica*, vol. 62, no. 6, pp. 106–112, 2013.

[12] Y. Li, T. Su, L. Z. Sheng, N. Xu, and B. S. Zhao, "Research on the X-ray wavelength division multiplexing technology for blackout region communication," *Optica Applicata*, vol. 50, no. 4, pp. 619–632, 2020.

[13] Y. Li, T. Su, L. Z. Sheng, N. Xu, and B. S. Zhao, "Simulation and experiment of X-ray communication in re-entry dusty plasma region," *Modern Physics Letters B*, vol. 34, article 2050057, no. 4, 2020.

[14] J. X. Mu, X. B. Tang, Y. P. Liu et al., "High penetration X-ray communication under physical shielding," *Journal of X-Ray Science and Technology*, vol. 28, no. 2, pp. 187–196, 2020.

[15] S. Lai, X. B. Tang, Y. P. Liu, J. X. Mu, Z. P. Feng, and K. Miao, "X-ray high frequency pulse emission characteristic and application of CNT cold cathode x-ray source cathode x-ray source," *Nanotechnology*, vol. 33, article 075201, no. 7, 2022.

[16] Y. Y. Wang, Y. P. Liu, J. X. Mu, and X. B. Tang, "Collimating/focusing optical system designed for hard X-ray communication," *Nuclear Instruments & Methods in Physics Research Section a-Accelerators Spectrometers Detectors and Associated Equipment*, vol. 1016, article 165776, 2021.

[17] S. Hang, X. B. Tang, H. Li, Y. P. Liu, J. X. Mu, and W. Zhou, "Novel approach for Mars entry blackout elimination based on X-ray communication," *Journal of Spacecraft and Rockets*, vol. 56, no. 5, pp. 1546–1552, 2019.

[18] W. Zhou, X. B. Tang, Y. P. Liu et al., "Power budget and performance analysis of X-ray communication during the Earth re-entry of spacecraft," *Optik*, vol. 199, article 163521, 2019.

[19] H. Li, X. B. Tang, S. Hang, Y. P. Liu, and D. Chen, "Potential application of X-ray communication through a plasma sheath encountered during spacecraft reentry into earth's atmosphere," *Journal of Applied Physics*, vol. 121, no. 12, pp. 277–289, 2017.

[20] H. Li, X. B. Tang, S. Hang, Y. P. Liu, J. X. Mu, and W. Zhou, "Re-entry blackout elimination and communication performance analysis based on laser-plasma-induced X-ray emission," *Physics of Plasmas*, vol. 26, article 033503, no. 3, 2019.

[21] J. Ma, G. Y. Lu, S. Y. Yu, L. Y. Tan, Y. L. Fu, and F. J. Li, "Acquisition performance analysis for intersatellite optical communications with vibration influence," *Chinese Physics B*, vol. 29, no. 1, pp. 330–336, 2020.

[22] V. Vilnrotter, D. Hoppe, B. Moision, and J. Charles, "Optical communications performance of hybrid 34-meter microwave antennas," in *2010 IEEE Aerospace Conference*, pp. 1–13, Big Sky, MT, USA, 2010.

[23] S. I. Sheikh, *The Use of Variable Celestial X-Ray Sources for Spacecraft Navigation*, University of Maryland, College Park: Ann Arbor, 2005.

[24] P. T. Chen, B. N. Zhou, J. L. Speyer, D. S. Bayard, W. A. Majid, and L. J. Wood, "Aspects of pulsar navigation for deep space mission applications," *The Journal of the Astronautical Sciences*, vol. 67, no. 2, pp. 704–739, 2020.

[25] A. A. Emadzadeh and J. L. Speyer, "On modeling and pulse phase estimation of X-ray pulsars," *IEEE Transactions on Signal Processing*, vol. 58, no. 9, pp. 4484–4495, 2010.

[26] J. E. Hanson, *Principles of X-Ray Navigation*, Standford University, CA, United States, 1996.

[27] Y. Mao, J. P. Chen, X. Y. Song, X. L. Jia, and X. B. Wu, "Attitude determination method of spacecraft using X-ray pulsars," *Science of Surveying and Mapping*, vol. 36, no. 6, pp. 8-9, 2011.

[28] C. Liu, X. K. Yue, K. K. Shi, and Z. W. Sun, *Spacecraft Attitude Control: A Linear Matrix Inequality Approach*, Elsevier, 2022.

[29] Y. S. Wang, Y. D. Wang, W. Zheng, M. Z. Song, and G. H. Li, "Stellar angle-aided pulse phase estimation and its navigation application," *Aerospace*, vol. 8, no. 9, p. 240, 2021.

[30] Y. S. Wang, Y. D. Wang, and W. Zheng, "On-orbit pulse phase estimation based on CE-Adam algorithm," *Aerospace*, vol. 8, no. 4, pp. 1–14, 2021.

[31] N. Moriya, Y. Sano, H. Suzuki, and K. Iwamoto, "Optical Collimator, Optical Connector Using Same, and Holding Member for Optical Collimator," Europe Patent EP11768750, 2011.

[32] H. Zhang, R. Jiao, and L. P. Xu, "Orbit determination using pulsar timing data and orientation vector," *Journal of Navigation*, vol. 72, no. 1, pp. 155–175, 2019.

[33] L. Geng, X. Ma, Z. T. Xiao, F. Zhang, F. Rong, and X. S. Peng, "Calibration and filtering of X-ray line array detector," *Infrared and Laser Engineering*, vol. 46, no. 12, pp. 293–300, 2017.